Structural and Functional Abnormalities of Retinal Ganglion Cells Measured In Vivo at the Onset of Optic Nerve Head Surface Change in Experimental Glaucoma

Brad Fortune, Claude F. Burgoyne, Grant A. Cull, Juan Reynaud, and Lin Wang

Purpose. To compare peripapillary retinal nerve fiber layer thickness (RNFLT), RNFL retardance, and retinal function at the onset of optic nerve head (ONH) surface topography change in experimental glaucoma (EG).

Methods. Thirty-three rhesus macaques had three or more weekly baseline measurements in both eyes of ONH surface topography, peripapillary RNFLT, RNFL retardance, and multifocal electroretinography (mfERG). Laser photocoagulation was then applied to the trabecular meshwork of one eye to induce chronic elevation of IOP and weekly recordings continued alternating between ONH surface topography and RNFLT during one week and RNFL retardance and mfERG the next week. Data were pooled for the group at the onset of ONH surface topography change in each EG eye, which was defined as the first date when either the mean position of the disc (MPD) fell below the 95% confidence limit of each eye's individual baseline range and/or when the topographic change analysis (TCA) map was subjectively judged as having demonstrated change, whichever came first. Analysis of variance with post hoc tests corrected for multiple comparisons were used to assess parameter changes.

Results. At onset of ONH surface topography change, there was no significant difference for RNFLT versus baseline or fellow control eyes. RNFL retardance and mfERG were significantly reduced in the recordings just prior (median of 9 days) to ONH onset ($P < 0.01$) and had progressed significantly ($P < 0.001$) an average of 17 days later (median of 7 days after ONH onset). RNFLT did not exhibit significant thinning until 15 days after onset of ONH surface topography change ($P < 0.001$).

Conclusions. These results support the hypothesis that during the course of glaucomatous neurodegeneration, axonal cytoskeletal and retinal ganglion cell functional abnormalities exist before thinning of peripapillary RNFL axon bundles begins. (*Invest Ophthalmol Vis Sci.* 2012;53:3939–3950) DOI: 10.1167/iovs.12-9979

From the Devers Eye Institute, Discoveries in Sight Research Laboratories, Legacy Research Institute, Legacy Health, Portland, Oregon.

Supported by National Institutes of Health Grants R01-EY019327 (BF), R01-EY011610 (CFB), and R01-EY019939 (LW); Glaucoma Research Foundation (BF); American Health Assistance Foundation (BF); Legacy Good Samaritan Foundation; Heidelberg Engineering, GmbH, Heidelberg, Germany (equipment and unrestricted research support); and Carl Zeiss Meditec, Inc. (equipment).

Submitted for publication April 5, 2012; accepted May 2, 2012.

Disclosure: **B. Fortune**, Carl Zeiss Meditec Inc. (F), Heidelberg Engineering, GmbH (F); **C.F. Burgoyne**, Heidelberg Engineering, GmbH (F); **G.A. Cull**, None; **J. Reynaud**, None; **L. Wang**, None

Corresponding author: Brad Fortune, Devers Eye Institute, 1225 NE Second Avenue, Portland, OR 97232; bfortune@deverseye.org.

Retinal nerve fiber layer (RNFL) defects have been recognized for decades as an important diagnostic sign of glaucoma, as they present clinically during an early stage and are predictive of subsequent vision loss.[1–3] However, the minimum loss of RNFL detectable by traditional clinical methods such as ophthalmoscopy and photography may be 50 to 70 μm, or as much as 50% of the normal tissue thickness.[4,5] Thus, it is hoped that recent advancements in imaging techniques will improve glaucoma detection and management by providing reliable, sensitive, and quantitative measurements of the RNFL.[6,7]

The two techniques used most commonly for this purpose are scanning laser polarimetry (SLP)[8] and optical coherence tomography (OCT).[9] Confirming earlier findings, both of these techniques have been used to demonstrate that lower baseline RNFL values are predictive of future glaucoma progression, including loss of vision.[10,11] Yet the optical principles underlying these two techniques differ in potentially important ways. OCT measures the relative time-of-flight delay of a (typically) near infrared source after it is reflected by structures at different depths within the tissue sample.[12,13] OCT thus can provide a high-resolution cross-sectional image of retinal layers and an estimate RNFL thickness (RNFLT) by detecting the relatively steep reflectance transition at both its anterior and posterior limits. In contrast, SLP estimates RNFL "thickness" indirectly by measuring the relative phase retardance of orthogonally polarized states of the imaging source after a double pass through the tissue sample.[8] RNFL retardance is caused by form birefringence, an optical property thought to be due—in the case of the RNFL—to the orderly parallel structural array of thin cylindrical cytoskeletal components within retinal ganglion cell (RGC) axons, primarily the microtubules (MTs), and to a lesser extent neurofilaments.[14–16] Empirical evidence supporting this original theoretical framework includes studies demonstrating that RNFL birefringence declines rapidly after chemical disruption of MTs in situ[16] and in vivo.[17] Thus, it has been suggested that measurements of RNFL birefringence could provide a sensitive indicator of compromised cytoskeleton integrity within RGC axons.[16–18] The importance of this idea is underscored by evidence of axonal cytoskeletal changes occurring in experimental models of glaucoma, including their earliest stages,[19–23] some of which may represent mechanisms of further susceptibility.[24,25]

RNFL birefringence can be assessed in a clinical setting either directly, such as by polarization-sensitive OCT,[26–29] or it can be inferred by comparing SLP measurements of RNFL retardance with OCT measurements of RNFLT.[17] In one such experiment, we demonstrated that RNFL retardance began to decline prior to and to progress faster than RNFL thinning after an experimental RGC injury by retrobulbar optic nerve transection.[30] This early stage structural abnormality was also associated with specific loss of RGC function as measured by electroretinography (ERG). The results of that study provided clear evidence for the

Table 1. Study Subjects Age, Weight, Sex, and IOP Information

Animal ID	Age (years)	Sex	Weight (kg)	Duration, First Laser to ONH Onset (weeks)	Control Mean IOP (mmHg)	EG Mean IOP (mmHg)	Control Peak IOP (mmHg)	EG Peak IOP (mmHg)	Cumulative IOP Difference (mmHg × days)
21676	12.5	F	5.4	32	10.9	12.2	18.0	30.0	315.5
22906	12.3	F	7.5	31	12.2	12.3	31.3	18.0	109.5
23499	9.9	F	4.9	15	11.4	12.9	15.3	21.3	122.2
23538	10.7	F	4.9	16	11.6	13.3	19.0	19.3	196.8
25357	2.6	M	5.5	27	8.8	9.9	13.3	23.0	157.5
25564	2.3	F	3.7	22	9.7	11.2	16.0	18.0	182.7
26072	1.5	F	4.1	27	8.8	9.1	15.3	16.3	60.9
26161	1.4	F	3.3	28	8.7	9.1	14.3	26.0	16.8
AM76	21.9	F	8.6	28	10.7	12.8	14.7	30.3	350.7
AM89	21.9	M	8.9	16	13.4	14.4	19.7	20.7	94.3
AO23	20.0	F	7.2	15	9.2	13.4	13.3	21.3	446.5
AP02	18.6	F	5.6	18	9.2	10.8	13.3	14.3	192.5
23506	12.5	F	4.5	6	11.6	18.7	15.0	46.3	190.7
23522	10.9	F	7.9	9	9.8	10.5	12.0	16.3	12.3
23532	11.1	F	5.0	5	11.8	12.1	16.3	20.3	−21.7
25354	4.3	M	4.8	12	9.9	11.1	13.0	20.0	106.3
25356	4.1	M	5.1	5	9.1	9.1	13.3	13.7	−19.3
25997	3.2	M	4.3	5	10.6	15.3	13.3	39.3	126.7
26163	3.2	M	4.2	5	9.6	9.3	12.0	17.0	−35.3
135	10.6	M	11.4	6	9.8	10.8	12.3	13.0	43.8
137	9.6	M	13.0	8	15.0	18.3	21.0	29.7	167.4
139	9.1	F	6.2	27	13.4	16.0	19.3	33.0	469.7
140	8.8	F	6.1	15	9.7	14.5	16.0	35.7	477.3
15527	21.4	F	8.5	7	13.4	17.3	17.7	35.0	196.7
22100	22.9	F	5.3	7	10.5	11.9	12.7	18.3	42.2
22159	20.0	F	8.2	7	9.3	10.1	12.0	17.3	25.0
22165	21.9	F	6.0	14	9.4	10.3	12.3	16.3	93.8
24369	5.8	F	6.7	9	9.1	9.5	14.0	14.3	−4.7
18664	15.3	F	5.9	16	8.5	10.4	12.3	15.3	204.0
19193	15.2	F	6.4	5	9.7	12.3	11.7	26.0	41.2
19211	14.2	F	5.9	13	11.1	12.9	19.3	27.3	190.7
20457	13.5	F	7.1	10	10.3	19.9	13.7	53.7	907.2
13904	15.4	F	5.7	23	13.0	13.5	20.0	28.7	−24.3
Average	11.8	25 F	6.3	14.9	10.6	12.6	15.5	24.1	164.7
SD	6.8	8 M	2.1	8.8	1.6	2.9	4.0	9.8	193.5

existence of an early stage of RGC degeneration when both axonal cytoskeletal abnormalities and RGC functional abnormalities are found in the absence of significant thinning of axon bundles within the RNFL.[30] Though optic nerve transection and crush are classical experimental models of axonal injury within the central nervous system, they represent a more acute and rapid process as compared with the neurodegenerative course of glaucoma. Therefore, the aim of this study was to test the same hypothesis in a nonhuman primate model of experimental glaucoma. Longitudinal measurements of RNFL retardance obtained by SLP and ERG measures of retinal function were compared with RNFLT measurements made by OCT and specifically evaluated an early stage of experimental glaucoma as defined by the onset of optic nerve head (ONH) surface topography change. This time point was chosen because it is thought to represent a very early stage of experimental glaucoma in nonhuman primates.[31–33]

Methods

Subjects

The subjects of this study were 33 rhesus macaque monkeys (*Macaca mulatta*). Table 1 lists the age, weight, and sex of each animal. All experimental methods and animal care procedures adhered to the Association for Research in Vision and Ophthalmology's Statement for the Use of Animals in Ophthalmic and Vision Research and were approved and monitored by the Institutional Animal Care and Use Committee at Legacy Health.

Anesthesia

All experimental procedures began with induction of general anesthesia using ketamine (15 mg/kg IM) in combination with either xylazine (0.8–1.5 mg/kg IM) or midazolam (0.2 mg/kg IM), along with a single subcutaneous injection of atropine sulphate (0.05 mg/kg). Animals were then intubated and breathed 100% oxygen for retinal function testing by ERG, during which anesthesia was maintained using a combination of ketamine (5 mg/kg/hr IV) and xylazine (0.8 mg/kg/hr IM). Upon completion of retinal function testing, ketamine-xylazine administration was discontinued and isoflurane gas (1%–2%) was mixed with oxygen to provide anesthesia during SLP scan acquisition. Anesthesia for all other structural imaging sessions (see below) was maintained using isoflurane gas (1%–2%; typically 1.25%) via endotracheal tube. During all procedures, heart rate and arterial oxyhemoglobin saturation were monitored continuously and maintained above 75/min and 95%, respectively. Body temperature was maintained at 37°C.

ONH Surface Topography

ONH surface topography was measured by confocal scanning laser tomography (CSLT; Heidelberg Retina Tomograph II, Heidelberg Engineering GmbH, Heidelberg, Germany) as recently described.[34] A minimum of three individual scans were acquired at each CSLT imaging session and averaged to create a mean topography for each eye. All CSLT scans were performed 30 minutes after IOP was manometrically lowered to 10 mmHg because the ambient IOP level is known to significantly influence ONH structure and surface topography.[31,35–37] Thus, elastic deformation of ONH tissues due to IOP elevation existing at the start of any given imaging session was eliminated, leaving primarily only the permanent changes to influence the topography.[32]

A trained technician outlined the optic disc margin within the baseline image of each eye using a disc photograph for reference where necessary; this contour line was automatically transferred to all subsequent images in the longitudinal series. For the current study, the parameter mean position of the disc (MPD) was calculated for each CSLT session as described previously.[35] Briefly, MPD refers to the height of the surface of the ONH (i.e., average height of all pixels located within the disc margin contour line) relative to the height of a reference plane (320 μm).[38] The MPD value used in this analysis was derived from the averaged topography. All CSLT scans in this study had an acceptable quality score whereby the mean pixel height standard deviation was 40 or less (99.5% were $\leq$30; 92% were $\leq$20).

Peripapillary RNFL Thickness

Peripapillary RNFLT was measured using spectral domain OCT (SD-OCT, Spectralis; Heidelberg Engineering GmbH). For this study, the average peripapillary RNFLT was measured from a single circular B-scan consisting of 1536 A-scans. Nine to 16 individual sweeps were averaged in real time to comprise the final stored B-scan at each session. The position of the scan was centered on the ONH at the first imaging session and all follow-up scans were pinned (identical) to this location. A trained technician manually corrected the accuracy of the instrument's native automated layer segmentations when the algorithm had obviously erred from the inner and outer borders of the RNFL to an adjacent layer (such as a refractive element in the vitreous instead of the internal limiting membrane, or to the inner plexiform layer instead of the outer border of the RNFL). All segmentations were then exported for extraction of RNFLT values by custom software. All SD-OCT scans in this study had an acceptable quality score above 15 (99% were $\geq$20; 50% were $\geq$30).

Peripapillary RNFL Retardance

Peripapillary RNFL retardance measurements were obtained by SLP (GDxVCC; Carl Zeiss Meditec, Inc., Dublin, CA) as previously described.[30,39,40] The instrument compensates for the effects of anterior segment (primarily corneal) birefringence to more accurately determine RNFL birefringence.[41,42] Thus, anterior segment birefringence measurements are obtained prior to initial baseline RNFL scans, then used to compensate all subsequent RNFL scans. A bite-bar, which rotates in three axes, was used to properly align the head and eye, and autorefraction is used for each scan. Three RNFL scans were averaged for each eye at each time point.

The SLP instrument detects the relative phase retardance of a cross-polarized source after a double pass through the tissue sample, assumes that RNFL thickness is linearly related to retardance, then calculates and reports an estimate of RNFL "thickness" using a linear conversion factor of 0.67 nm/μm[8] (as stated in the instrument manual[43]). Values of RNFL thickness were exported for the "small" peripapillary locus, which is an 8-pixel wide band centered on the optic disc with a mean scan radius of 4.84°,[43] corresponding to about 1.12 mm on the macaque retina.[30] After conversion back to units of retardance, the average of the 64 exported peripapillary samples was taken as the summary parameter for each eye and time point.

Assessment of Function

Retinal function was evaluated by multifocal ERG (mfERG) as previously described.[30,44,45] Briefly, mfERGs were recorded using a multifocal system (VERIS; Electro-Diagnostic Imaging, Inc., Redwood City, CA). The mfERG stimulus consisted of 103 unscaled hexagonal elements subtending a total field size of ~55°. The luminance of each hexagon was independently modulated between dark (1 cd/m^2) and light (200 cd/m^2) according to a pseudorandom, binary m-sequence. The temporal stimulation rate was slowed by insertion of 7 dark frames into each m-sequence step ("7F"). The m-sequence exponent was set to 12, thus the total duration of each recording was 7 minutes, 17 seconds. Signals were amplified (gain = 100,000); band-pass filtered (10–300 Hz; with an additional 60-Hz line filter); sampled at 1.2 kHz (i.e., sampling interval = 0.83 ms); and digitally stored for subsequent offline analyses. Two such recordings were obtained for each eye at each time point and averaged.

From the average of the two recordings at each time point, a subset of local responses from the full array, limited to the central element and the three rings surrounding it (37 local responses in total), was processed to derive summary outcome parameters. A high-pass filter (5-pole, >75 Hz) was applied to each local mfERG response to extract the high frequency components (HFC). The low frequency component (LFC) of each response was represented as the raw response minus the HFC. The amplitude of the HFC was calculated as the root mean square (RMS) for the epoch between 0–80 ms of each filtered record. Peak amplitudes for LFC features were quantified as follows: the first negative feature (N1) was calculated as the maximum negative excursion from baseline in the epoch up to 30 ms; the amplitude of the first positivity (P1) was calculated as the voltage difference between the maximum peak and the N1 trough; and the second negativity (N2) was calculated as the difference between baseline and the minima from 30–80 ms. The global average (of 37 response locations) for each parameter represented the measurement for each eye at each ERG session.

IOP Measurements

IOP was measured in both eyes at the start of every session using an applanation tonometer (Tono-Pen XL; Reichert Technologies, Inc., Depew, NY). The value recorded for each eye was the average of three successive measurements.

Experimental Design and Protocol

Each animal had a minimum of three (average of 5) weekly baseline recordings for each of the above-described measurements. Argon laser photocoagulation was then applied to the trabecular meshwork of one eye of each animal to induce chronic elevation of IOP.[46,47] Initially, 180° of the trabecular meshwork was treated in one session, then the remaining 180° was treated in a second session approximately 2 weeks later. If necessary, laser treatments were repeated in subsequent weeks (limited to a 90° sector) until an IOP elevation was first noted or if the initial post-laser IOP had returned to normal levels. The average number of laser treatments ($\pm$SD) was 5.6 $\pm$ 3.2.

Weekly measurements continued during the post-laser follow-up period in alternating fashion such that CSLT and SD-OCT scans were acquired during a single session in 1 week, then ERG and SLP during the next week. Thus, each measurement (within a given type) was separated by approximately 2 weeks. This schedule continued for each animal until its predefined study endpoint had been reached. Specific endpoints were based on the primary study to which each animal was assigned and were determined based on those specific protocols. Thus, the specific endpoint targets and details of sacrifice procedures differed across animals.

For this study, however, the time point of interest was the onset of ONH surface topography change from baseline, which is thought to represent a very early stage of experimental glaucoma in nonhuman primates.[31–34,36] This time point was determined using two parameters from the CSLT data for each animal as follows. The 95% confidence limits of baseline variability were calculated for the MPD parameter in

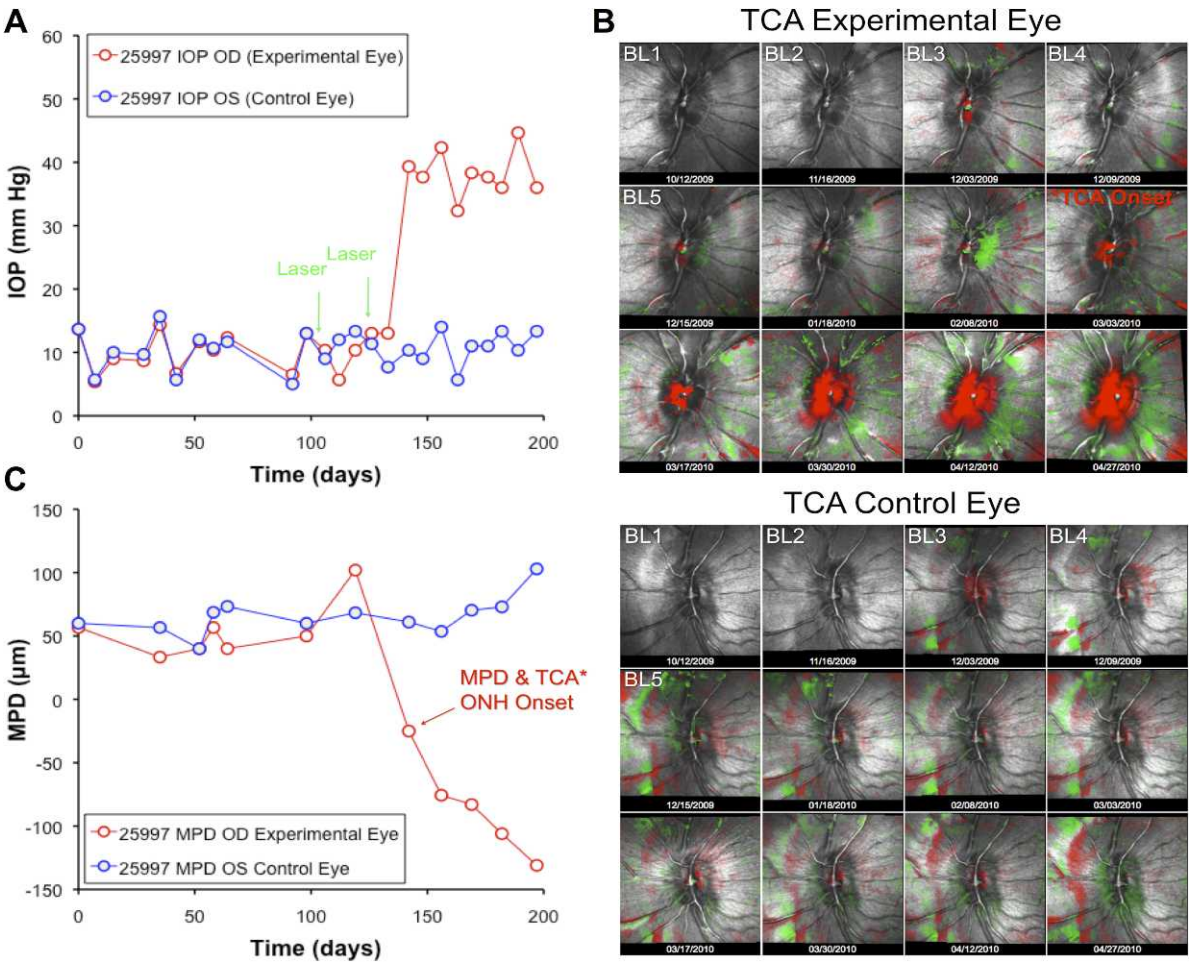

Figure 1. Example of experimental time course for a single representative animal. (**A**) IOP versus time. *Green arrows* indicate dates of trabecular meshwork laser photocoagulation. (**B**) ONH surface topography over time, with TCA showing significant posterior (*red pixels*) and anterior (*green pixels*) deformation as compared with baseline (BL). (**C**) The CSLT parameter MPD versus time.

each eye. The first observation (longitudinal time point) at which the MPD parameter fell below the lower limit of baseline variability with two sequential confirmatory observations served as the MPD change onset point. ONH surface topography change was also evaluated using topographic change analysis (TCA)[48,49] in masked subjective fashion by one of the authors (CFB) on two separate occasions separated by 2 or more months; any difference between successive judgments was adjudicated with a second reader (BF). For this study, the onset of ONH surface topography change was defined as the earlier date between the two change indicators (MPD or TCA).

The SD-OCT, SLP, and ERG results were then grouped together ($N =$ 33 EG eyes and $N = 33$ fellow control eyes) at baseline (three baseline time points each, chosen randomly when more were available) and at the onset of ONH surface topography change for each EG eye. Since SD-OCT and CSLT scans were always acquired in the same session, the ONH surface change onset point coincided with an RNFLT measurement in each eye, but was separated by ~1 week from the next nearest RNFL retardance (SLP) and retinal function (ERG) measurement; thus, the latter are grouped by the next nearest session available immediately prior to and immediately after the ONH onset point. Figure 1 provides an example of the longitudinal course for one individual animal.

Statistics

Data are represented by box plots, which indicate the median, interquartile range, and extremes (hashmarks) of the grouped data at each time point. Two-way analysis of variance for repeated-measures was used to test the effects of the treatment group (EG versus control) and time with an interaction term (Prism 5; GraphPad Software, Inc., La Jolla, CA). Post hoc tests of differences between groups and/or time points were performed as paired *t*-tests with Bonferroni's correction for multiple comparisons.

Results

Table 1 lists the IOP results for each individual animal as well as the group averages and standard deviations. The mean IOP values listed for each animal represent the average of all observations between the date of the first laser treatment in the EG eye and the date of ONH surface topography change in that eye; the peak values represent the peak observed within that same span. The data in Table 1 show that chronic IOP elevation was modest: post-laser mean IOP in EG eyes was only 2 mmHg higher, on average, than the mean IOP in fellow control eyes. The peak IOP observed in EG eyes was just under 10 mmHg higher than the peak observed in the fellow control eyes, on average. Only 2 of the 33 EG eyes had a peak IOP measured above 40 mmHg prior to onset of ONH surface topography change.

Figure 1 provides an example of the experimental course for a single individual animal. IOP is plotted against time in panel A; steady IOP elevation occurred after two laser sessions in the treated eye. Panel B displays CSLT results for the EG eye

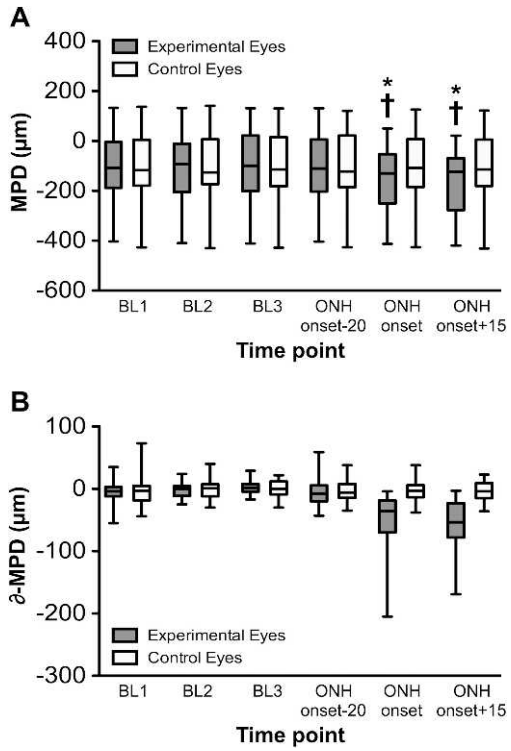

Figure 2. (**A**) The CSLT parameter MPD versus time for entire group. Box plots represent distribution of MPD values (median, interquartile range, and extremes) for the three BL sessions as well as the session where ONH surface topography onset occurred for each EG eye and the next nearest session prior to and after ONH surface topography onset (which occurred a median of 20 days prior and 15 days after ONH surface change onset, respectively). (**B**) MPD values normalized to the BL average for each eye and plotted as the difference from BL versus time. *$P < 0.0001$ versus each BL; †$P < 0.0001$ versus the session just prior to ONH onset (median of 20 days prior).

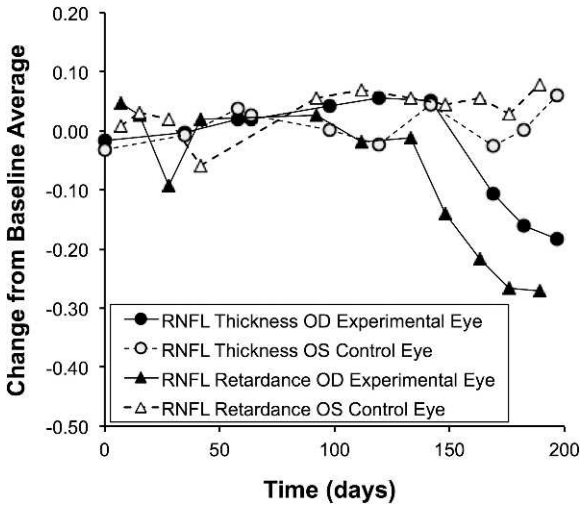

Figure 3. RNFL retardance and thickness versus time for the individual example animal shown in Figure 1. SLP measurements of RNFL retardance and SD-OCT measurements of RNFL thickness are normalized to the baseline average and plotted versus time as change from baseline.

(*top series* of 12 images) and control eye (*bottom series*). Overlaid on the reflectance images are the TCA results with red superpixels representing significant posterior displacement and green superpixels representing significant anterior displacement as compared with the first baseline topography. This animal had five pre-laser baseline sessions across which the TCA retest variability can be assessed. The result of masked subjective TCA analysis in this eye indicated that the onset of ONH topographic change occurred on day 142 (36 days after the first trabecular laser). Quantitative analysis of the CSLT data using the parameter MPD (Fig. 1C) also indicated that onset of topographic change occurred at day 142. Thus, day 142 was chosen as the ONH topography change onset point for this animal. In 14 of the 33 animals, TCA and MPD analysis identified the onset point as being on the same date. In 17 animals, the date indicated by TCA was earlier; in 2 animals, the date indicated by MPD was earlier. The average difference was 28 ± 48 days earlier for TCA.

Figure 2 shows the longitudinal MPD results for the entire group; the raw data was plotted in Figure 2A and normalized data in Figure 2B. Data are shown for three (randomly selected) baseline sessions as well as from the session identified in each eye as the onset of ONH topography change and the next nearest session both prior to and immediately subsequent to the ONH onset date. The median duration between ONH onset and the CSLT session immediately prior to onset was 20 days, while the median duration from onset to the next CSLT session after onset was 15 days. The time point indications along the abscissa in Figure 1 (and all subsequent figures) reflect these values.

Figure 2A shows that the distribution of MPD values is repeatable over the three baseline sessions. There was a significant effect of time ($P < 0.0001$) and a time × treatment group interaction ($P < 0.0001$), with post hoc tests revealing that the EG group mean MPD at ONH onset was significantly lower (the ONH surface was significantly more posterior, $P < 0.0001$) than at each of the baseline sessions for that group as well as compared with the post-laser session immediately prior to onset (~20 days prior). When the MPD values were normalized to the average baseline value and plotted as change from baseline (Fig. 2B), it became clear that MPD varied by as much as ±50 μm (95% confidence interval) in the absence of glaucomatous deformation or axon loss and despite manometric IOP control at the time of CSLT imaging. The average MPD change at ONH onset in EG eyes was −51 μm (±45); consistent with the fact that in about half of the EG eyes, onset of ONH surface topography change was detected earlier by TCA than by MPD. There were no significant differences found across time points in the control eye group.

Figure 3 plots the average peripapillary values for RNFL thickness and RNFL retardance versus time for the same individual animal shown in Figure 1. The open symbols represent the longitudinal series for the control eye, filled symbols for the EG eye. It is clear that RNFL retardance as derived from the SLP measurements (*solid triangles*) began to decline shortly after the chronic IOP elevation ensued but prior to any RNFL thinning as measured by SD-OCT (*solid circles*). At MPD onset in this EG eye (day 142, see Fig. 1), RNFL thickness was essentially unchanged from baseline (4% thicker), whereas RNFL retardance was 15% below its baseline average value in the very next SLP measurement session (6 days later). The decline of RNFL retardance continued to lead the decline of RNFL thickness for the duration of follow-up in this animal.

Longitudinal results for peripapillary RNFL thickness and RNFL retardance are shown for the entire group in Figure 4. For RNFL thickness (Fig. 4A), there was a significant interaction ($P < 0.0001$)—that is, the effect of time ($P = 0.0001$) differed between the EG and control eye groups. This was confirmed by post hoc analysis, which revealed that RNFL

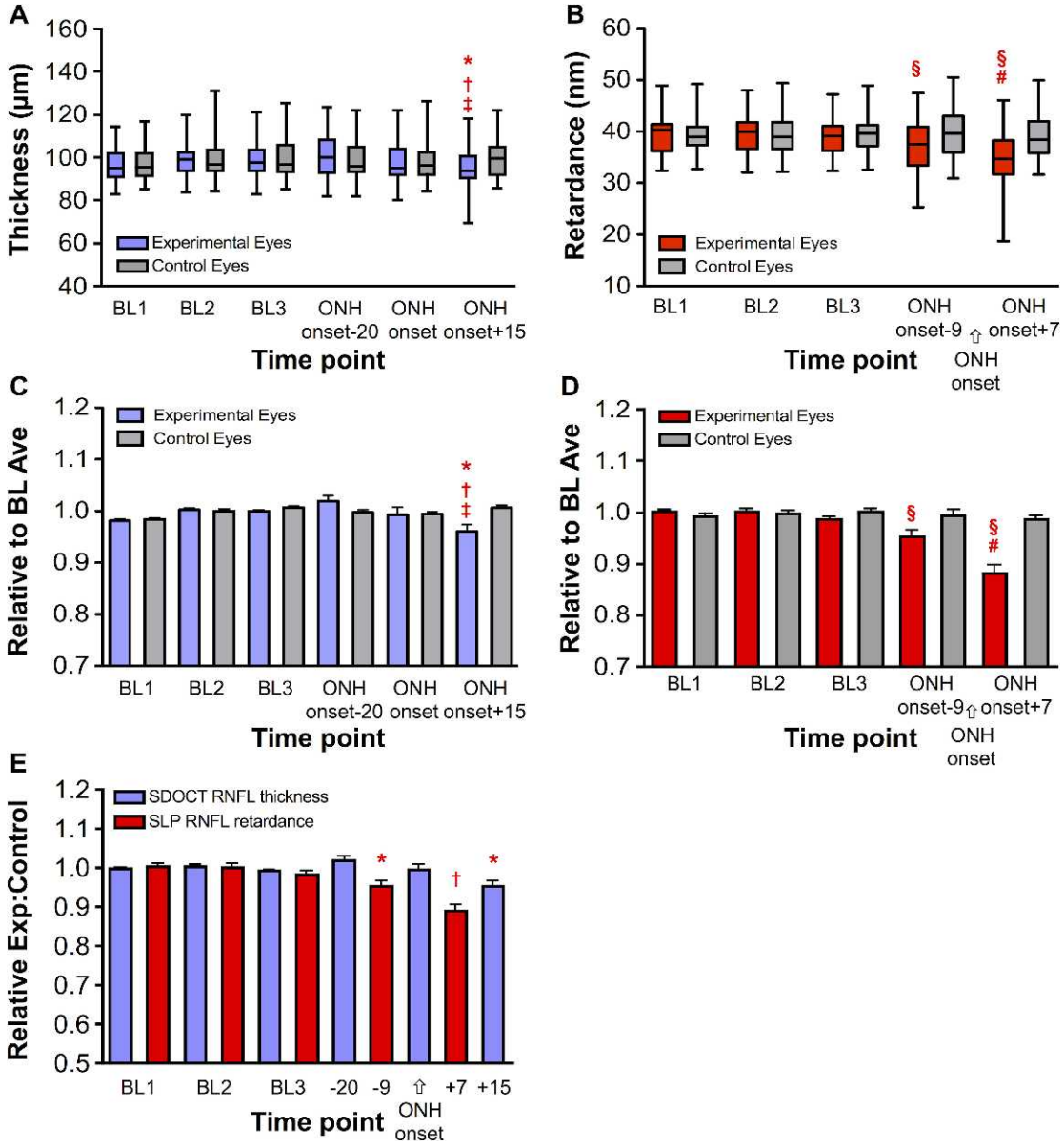

Figure 4. Box plots (as in Fig. 2) representing the distribution of raw values at each of the experimental recording sessions. (**A**) RNFL thickness. (**B**) Retardance. Values normalized to BL average are plotted in (**C**) and (**D**), respectively. (**E**) RNFL values for EG eyes—expressed relative to fellow control eye of each animal—versus time. For RNFL thickness data: $^*P < 0.001$, versus each BL; †$P < 0.05$ versus ONH surface topography onset; ‡ $P < 0.0001$ versus the session prior to ONH onset (median of 20 days prior). For RNFL retardance data: §$P < 0.01$ versus each BL; #$P < 0.0001$ versus each BL and the session just prior to ONH onset (median of 9 days prior). (**E**): $^*P < 0.01$ versus each BL; †$P < 0.0001$ versus each BL and the session just prior to ONH onset (median of 9 days prior).

thickness was reduced in the EG eyes at the final time point (median of 15 days after ONH topographic change onset) as compared with each of the baseline sessions ($P < 0.001$), to the session just prior to ONH onset ($P < 0.0001$) and to the ONH topographic onset point itself ($P < 0.001$). However, there were no significant differences between RNFL thickness at the ONH topographic onset point and any of the baselines or the session just prior to onset (median of 20 days earlier). Control eye values of RNFLT did not change significantly across any of the time points.

Figure 4B shows that RNFL retardance changed significantly over time in the group of EG eyes ($P < 0.0001$, time and interaction) such that there was a significant decline during the session just prior to ONH topographic change onset (median of 9 days earlier) as compared with each of the baseline sessions ($P < 0.01$). The next available SLP measurement (median of 7 days after ONH topographic onset) also showed that RNFL retardance had declined compared with each baseline measurement ($P < 0.0001$) and had progressed significantly from the previous SLP measurement ($P < 0.0001$, median of 17 days earlier). Control eye values of RNFL retardance did not change significantly across any of the time points.

The raw data shown in Figures 4A and 4B were normalized to the baseline average to better show relative changes over time by accounting for the variability across animals at baseline. The baseline-normalized data for RNFL thickness and retardance are plotted in Figures 4C and 4D, respectively. This revealed a subtle trend for RNFL thickness: during the session just prior to ONH topographic onset, there was a 2% ± 6% *thickening* as compared with the baseline average;

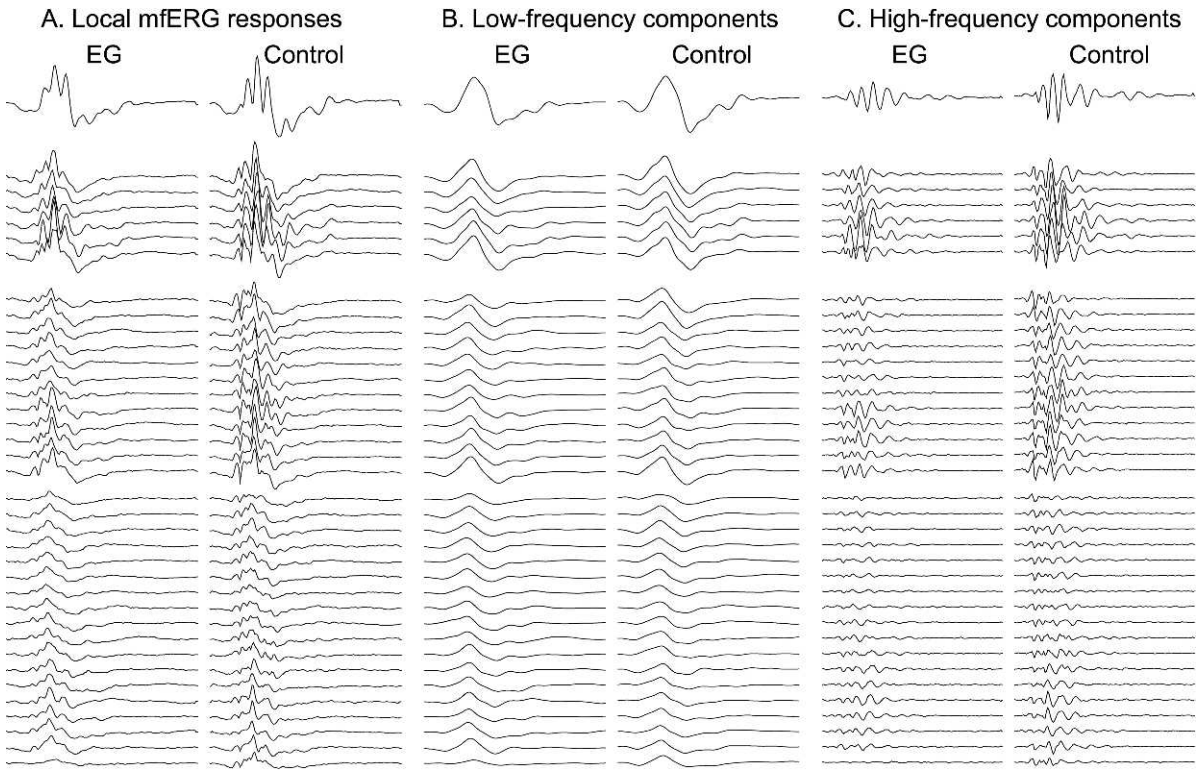

Figure 5. Multifocal ERG responses from the final recording session of the same individual animal shown in Figures 1 and 3. The first pair of columns (**A**) shows the local mfERG responses for the EG eye (*left*) and control eye (*right*); the middle pair of columns (**B**) contains the low-frequency components and the rightmost pair of columns (**C**) contains the high-frequency components filtered from the local responses. The top row of traces represents the response from the central stimulus element; the second group represents the first ring of responses around the center, and so on. These 37 response locations represent the data used to generate the spatially averaged summary parameter as described in the Methods section and shown in Figures 6 and 7.

however, this was not statistically significant. The only significant difference found for RNFLT was at the final time point, which represented a 4% ± 7% thinning as compared with baseline ($P < 0.01$), as well as a significant decrease compared with the point ONH topographic onset ($P < 0.05$) or to the session just prior to ONH onset ($P < 0.0001$). Again, there were no significant differences over time for the group of control eyes. Baseline normalization of the RNFL retardance data (Fig. 4D) demonstrate a pattern of significant change in the group of EG eyes ($P < 0.0001$, effects of time and time × treatment interaction), whereby there was a 5% ± 8% decline from baseline values of RNFL retardance during the session prior to ONH topographic change onset (9 days before onset, $P < 0.01$) and a significantly progressive decline to the next session reaching 12% ± 9% below the baseline average ($P < 0.0001$). There were no significant differences found across time points in the control eye group.

In order to visualize the relative changes more readily on a single plot, the EG group data for each measurement type were normalized relative to the control eye values as shown in Figure 4E. There was a significant effect of time ($P < 0.0001$), measurement type (RNFL thickness vs. retardance, $P = 0.0005$) as well as a significant interaction between those two variables ($P < 0.0001$). During the span of a month around the onset of ONH surface topography change, relative RNFL retardance can be seen to decline prior to and faster than RNFL thickness. The only significant difference found over time for relative RNFL thickness was at the final time point, approximately 2 weeks after ONH topography onset, when RNFLT was 5% ± 8% thinner than fellow control eyes ($P < 0.01$ versus each of the other time points). In contrast, approximately 1 month earlier, RNFL retardance had already become 5% ± 8% lower than fellow control eyes ($P < 0.01$ versus each baseline) and in the week before the final time point, it had declined farther to reach 11% ± 10% below fellow control eye values. Thus, the pattern shown in Figure 4E for the EG group data is quite similar to the individual EG shown in Fig. 3.

Figure 5 shows the mfERG responses from the final recording session of the same individual animal shown in Figures. 1 and 3. The first pair of columns (Fig. 5A) shows the local mfERG responses for the EG eye (*left*) and control eye (*right*); the middle pair of columns (Fig. 5B) contains the low-frequency components and the rightmost pair of columns (Fig. 5C) contains the high-frequency components (HFC) filtered from the local responses. The top row of traces represents the response from the central stimulus element; the second group represents the first ring of responses around the center, and so on. These 37 response locations represent the data used to generate the spatially averaged summary parameter as described in the Methods section. Note that the HFCs from the EG eye are reduced as compared with the fellow control eye responses at this final recording session, without much effect on the low-frequency components. The spatial average values for each of the four response components analyzed are plotted versus time for this animal in Figure 6. It is clear from Figure 6D that the HFCs in the EG eye begin to decline right around the onset of ONH surface topography change (day 142; see Fig. 1). In contrast, the three features measured in the LFCs, N1, P1, and N2 (Figs. 6A, 6B, and 6C, respectively) do not show the degree of change evident in the HFCs, though perhaps N2 was trending below the response average in the fellow control eye.

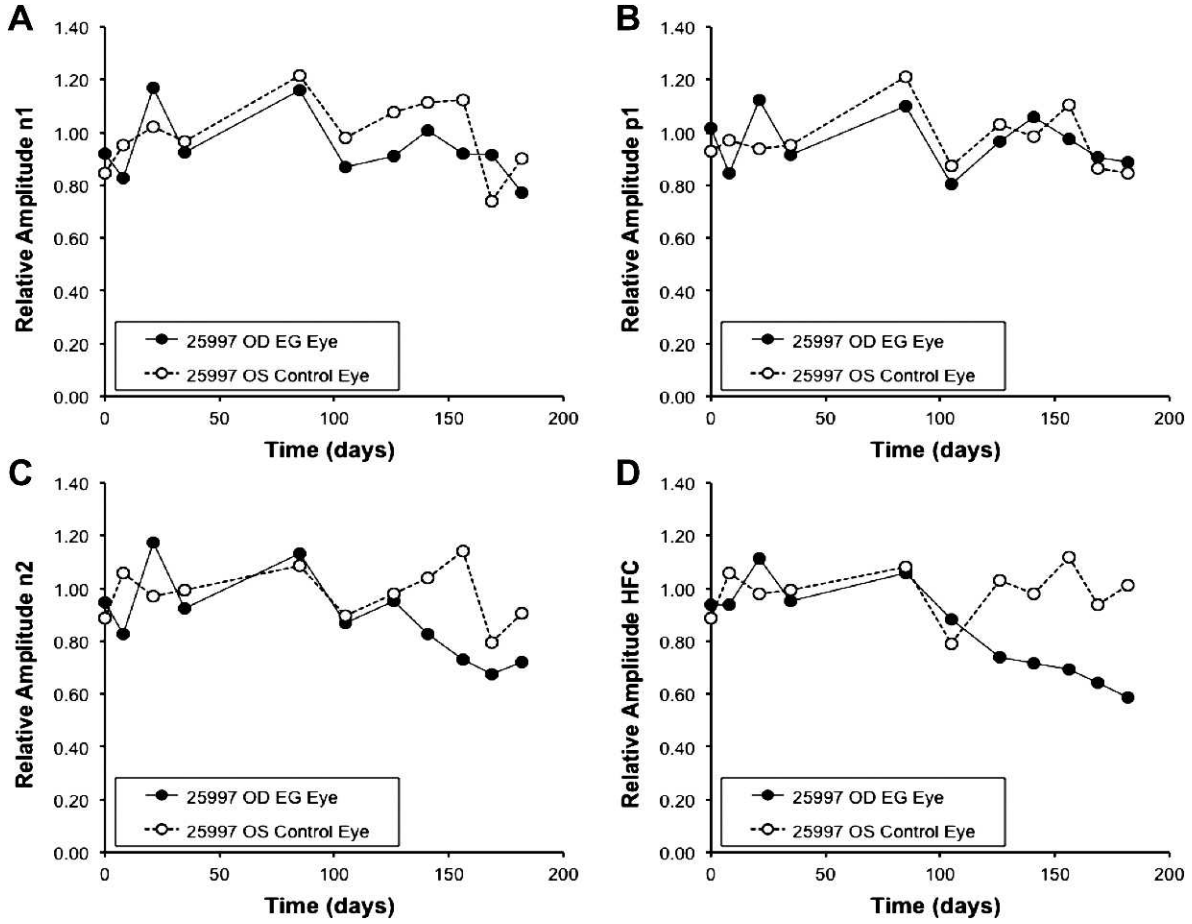

Figure 6. Multifocal ERG response component amplitudes versus time for the same individual example animal shown in Figures 1, 3, and 5. Data are normalized and plotted relative to the baseline average. (**A**) LFC features N1. (**B**) P1. (**C**) N2. (**D**) HFC.

The mfERG data for the entire group are plotted in Figure 7 for the same five time points that corresponding to the SLP recording sessions (e.g., Fig. 4). There was a significant effect of time and an interaction with the eye group ($P < 0.0001$ and $P = 0.001$, respectively) for the HFCs, but none of the other LFC features showed a significant effect of time nor a significant time treatment interaction ($P = 0.53$, 0.29, 0.31, for N1, P1, and N2 amplitudes, respectively). The mfERG HFCs were reduced at the time point just prior to onset of ONH surface topography change ($P < 0.01$ versus each baseline) and demonstrated significant progression to the session immediately subsequent to the ONH surface topography onset point ($P < 0.001$). There were no significant differences found across time points in the control eye group.

Discussion

The results of this study demonstrate that abnormalities of RNFL retardance measured by SLP are present at (or before) the onset of ONH surface topography change when RNFL thinning as measured by SD-OCT has not yet begun to occur. The results also demonstrate that mfERG abnormalities representing specific RGC functional deficits[30,44,45,50] are present at (or before) the onset of ONH surface topography change. Taken together, these results indicate that specific structural and functional abnormalities exist prior to the onset of thinning of the peripapillary RFNL axonal bundles in nonhuman primate experimental glaucoma. These results match the pattern of changes observed after optic nerve transection, a more acute RGC axonal injury with a faster time course of neurodegeneration.[30] The results provide further evidence of the existence of a stage of experimental glaucoma during which structural and functional abnormalities measurable in vivo by clinical instrumentation are present before axonal degeneration manifests as thinning of the unmyelinated axons within the RNFL. This stage is thus likely to precede RGC death, though this study did not specifically count RGC soma (follow-up post mortem histopathological studies are underway). In this regard, the abnormalities observed here might, in a clinical setting, serve as a "red flag" to advance therapy in glaucoma patients. It is not yet known, however, if the abnormalities documented here are reversible with therapy or if that would also prevent subsequent axonal degeneration manifested as thinning of the RNFL. Reversibility of retinal functional abnormalities as detected by pattern ERG after IOP was lowered has been demonstrated in glaucoma patients.[51,52]

The onset of ONH surface topography change is thought to represent a very early stage of experimental glaucoma in nonhuman primates.[31–33] Indeed, a previous study in a separate cohort of monkeys also demonstrated that RNFL thinning was not yet present at the onset of ONH surface topography change defined by CSLT in a similar manner.[34] However, the results of that study also demonstrated evidence of deep ONH structural changes detected by SD-OCT that were present at this early time point, suggesting that glaucomatous connective tissue changes within the laminar cribrosa and peripapillary sclera[32,33,53] might precede even the onset of

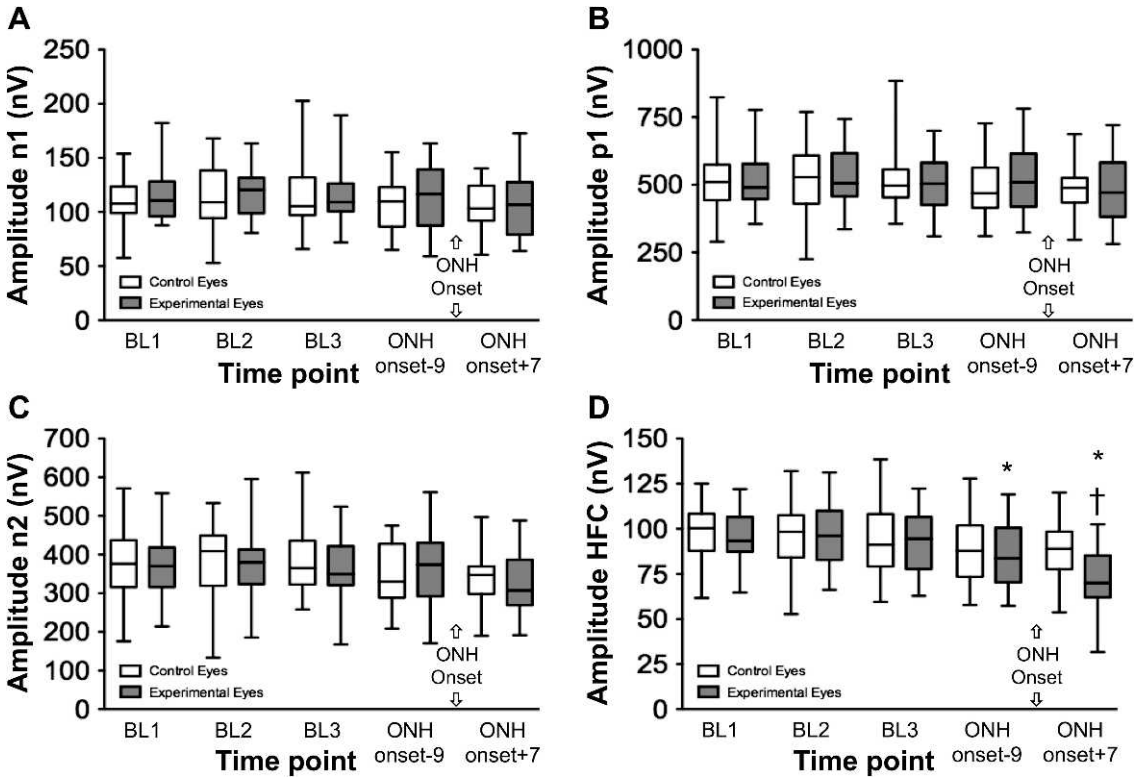

Figure 7. Multifocal ERG response component amplitudes versus time for the entire group. Box plots (as in Fig. 2) representing the distribution of raw values at each of the experimental recording sessions. (**A**) mfERG LFC features N1. (**B**) P1. (**C**) N2. (**D**) HFC. *$P < 0.01$ versus each BL. †$P < 0.001$ versus the session just prior to ONH onset (median of 9 days prior to ONH onset).

surface topography change.[34] Ongoing studies will address the course of those changes relative to the other early abnormalities demonstrated in this study by SLP and ERG. It should be noted that every EG eye in this study had exhibited ONH surface topography change by specific criteria, but not all eyes had reached RNFL or ERG change onset points by criteria with similar specificity. The study aimed to compare RNFL and ERG changes to each other (i.e., the ONH topography served as the common indicator and was therefore not meant to be compared to the other parameters).

There are several limitations to this study and caveats to discuss. First, the eccentricity of the measurement location (distance from the ONH) differed slightly for SLP and SD-OCT as the SLP location was 1.16° (~275 μm on the monkey retina) closer to the optic disc margin than the SD-OCT location. There is increasing evidence of retrograde degeneration in experimental glaucoma models in both rodents[25,54–58] and primates (Cull G, et al. *IOVS* 2011;52:ARVO E-Abstract 179) with retrobulbar axon counts revealing greater loss than either RNFLT or RGC soma counts do. If axons are dying by retrograde degeneration and there is otherwise no discrepancy between relative loss of RNFL retardance versus thickness, then this location mismatch could contribute to the apparent lead time of SLP retardance changes observed here. Though this is possible, the previous study of optic nerve transection matched the measurement locations as precisely as possible and still demonstrated a similar advance of RNFL retardance changes ahead of RNFL thinning.[30] That study included many fewer subjects and longitudinal time points, so it was feasible to accomplish the matching by manual techniques. Though it is also possible that gliotic or other changes within the RNFL could result in an increase in RNFLT, it is as yet unknown if such changes occur at this early stage or whether they could offset (nearly perfectly) any thinning or loss of axons.

A second caveat relates to the dynamic range of each measurement. This study using longitudinal data demonstrated that a decline in RNFL retardance and RGC function were detectable before any peripapillary RNFL thinning was detected by SD-OCT. At later time points, the relative loss of RNFL retardance (as compared with either baseline values or values in fellow control eyes) was greater than the relative loss of RNFLT. However, if their dynamic ranges were different, the relatively greater loss of RNFL retardance might not be as apparent. For example, there is a well-documented floor-effect for RNFLT at approximately 40% of normal values[59,60]; thus, judging decline from 100% of normal values would have a dynamic range limited to just 60% of the apparent range and any given loss might represent a larger actual loss for that parameter than the percent change would indicate. Since the floor effect asymptote is not yet known precisely for non-human primates (until enough animals can be followed to a severe stage), this question persists about the later time points when several parameters are exhibiting loss. Should these data become available, data could be re-scaled relative to the dynamic range of each parameter and thus be enable comparisons of relative loss across parameters on a similar scale.

Similarly, the relative measurement noise can vary across parameters; for example, by bootstrapping all possible pre-laser baseline pairs of observations, we found that the measurement noise for RNFL retardance by SLP is ~50% larger than that for RNFLT measured by SD-OCT (9% vs. 6%). If the inverse had been found, a stronger caveat would be necessary for the apparent lead time of detecting changes in retardance versus thickness; however, the results demonstrated earlier change for retardance, despite its larger measurement variability, suggesting the observation is robust.

It is possible that other ERG measures of RGC function and/or other analyses of the mfERG recordings presented in this study could reveal loss even more sensitively.[61,62] As in previous studies,[30,44,45] pattern-reversal ERG and full-field flash ERG (specifically to evaluate the photopic negative response) were also obtained in 21 of the 33 monkeys in this study but neither were able to reveal changes at this early time point (data not shown). Though the measurement variability was higher as compared with the mfERG HFCs, the lack of detection of RGC functional loss by these other techniques as compared with the mfERG could also be a function of the smaller sample size, so this study does not conclusively find that the mfERG was more sensitive per se.

Another caveat common to all experimental disease models is whether the results will prove generalizable to human patients in a clinical setting. Longitudinal clinical studies are underway at this and other institutions that will help determine whether the findings of this study are ultimately relevant to the care of glaucoma patients. The time course of EG in nonhuman primates is compressed (as is the life span of a monkey) compared with most glaucoma in human patients; thus longitudinal clinical studies require a substantially longer duration of follow-up, often complicated by changes in instrumentation reflecting technological improvements. Another important question for generalizability to clinical care will be the spatial relationships of RNFL changes: do the same temporal relationships between RNFL retardance and thickness hold not only for spatially averaged (global) parameters, but also sector by sector and also during later stages of neurodegeneration? Preliminary evidence suggests that RNFL retardance changes do continue to lead loss of RNFLT into subsequent stages of damage beyond the onset of ONH surface topography change (Fortune B, et al. *IOVS* 2012;53: ARVO E-abstract 240).

The rationale for this study evolved from the premise that axonal cytoskeletal disruption might be an early-stage alteration in the process of glaucomatous neurodegeneration, perhaps as a direct or indirect result of biomechanical changes within the ONH,[31–33,53] and exist for a time prior to the total degeneration of RGC axons. If true, then this might represent a phase during which advancement of therapy could be most efficacious (as compared with treatment after loss that would otherwise represent only permanent damage). If microtubule disruption is a large part of the cytoskeletal abnormality implied by these early changes in RNFL birefringence, then it is likely that axonal transport would also suffer at this early stage, potentially contributing further RGC insult.[20,21,56–58,63–68] There are otherwise very few studies that point to a specific stage detectable in a clinical setting of glaucomatous RGC "dysfunction" preceding death,[69–72] though more central changes in glaucoma[73] may complicate interpretation in some of these instances.

Finally, the visibility of axon bundles within the RNFL by clinical ophthalmoscopy and photography depends on their reflectance, which is also known to be greatly influenced by normal cytoskeletal integrity.[74] Thus, one might predict from the results presented here that reflectance should also decline prior to thickness[75–77] and that a degree of discordance should occur between photographic and SD-OCT methods of assessing the RNFL. Thus, clinical ophthalmoscopic and photographic methods should not be used as a reference standard to judge the diagnostic performance of methods like SLP and OCT.

Acknowledgments

The authors thank Galen Williams and Christy Hardin for their expert technical assistance during data collection.

References

1. Hoyt WF, Newman NM. The earliest observable defect in glaucoma? *Lancet*. 1972;1:692–693.
2. Hoyt WF, Frisen L, Newman NM. Fundoscopy of nerve fiber layer defects in glaucoma. *Invest Ophthalmol*. 1973;12:814–829.
3. Sommer A, Katz J, Quigley HA, et al. Clinically detectable nerve fiber atrophy precedes the onset of glaucomatous field loss. *Arch Ophthalmol*. 1991;109:77–83.
4. Quigley HA, Addicks EM. Quantitative studies of retinal nerve fiber layer defects. *Arch Ophthalmol*. 1982;100:807–814.
5. Quigley HA. Examination of the retinal nerve fiber layer in the recognition of early glaucoma damage. *Trans Am Ophthalmol Soc*. 1986;84:920–966.
6. Zangwill LM, Bowd C. Retinal nerve fiber layer analysis in the diagnosis of glaucoma. *Curr Opin Ophthalmol*. 2006;17:120–131.
7. Townsend KA, Wollstein G, Schuman JS. Imaging of the retinal nerve fibre layer for glaucoma. *Br J Ophthalmol*. 2009;93:139–143.
8. Weinreb RN, Dreher AW, Coleman A, Quigley H, Shaw B, Reiter K. Histopathologic validation of Fourier-ellipsometry measurements of retinal nerve fiber layer thickness. *Arch Ophthalmol*. 1990;108:557–560.
9. Huang D, Swanson EA, Lin CP, et al. Optical coherence tomography. *Science*. 1991;254:1178–1181.
10. Mohammadi K, Bowd C, Weinreb RN, Medeiros FA, Sample PA, Zangwill LM. Retinal nerve fiber layer thickness measurements with scanning laser polarimetry predict glaucomatous visual field loss. *Am J Ophthalmol*. 2004;138:592–601.
11. Lalezary M, Medeiros FA, Weinreb RN, et al. Baseline optical coherence tomography predicts the development of glaucomatous change in glaucoma suspects. *Am J Ophthalmol*. 2006;142:576–582.
12. Costa RA, Skaf M, Melo LA Jr., et al. Retinal assessment using optical coherence tomography. *Prog Retin Eye Res*. 2006;25:325–353.
13. Drexler W, Fujimoto JG. State-of-the-art retinal optical coherence tomography. *Prog Retin Eye Res*. 2008;27:45–88.
14. Zhou Q, Knighton RW. Light scattering and form birefringence of parallel cylindrical arrays that represent cellular organelles of the retinal nerve fiber layer. *Applied Optics*. 1997;36:2273–2285.
15. Huang XR, Knighton RW. Linear birefringence of the retinal nerve fiber layer measured in vitro with a multispectral imaging micropolarimeter. *J Biomed Opt*. 2002;7:199–204.
16. Huang XR, Knighton RW. Microtubules contribute to the birefringence of the retinal nerve fiber layer. *Invest Ophthalmol Vis Sci*. 2005;46:4588–4593.
17. Fortune B, Wang L, Cull G, Cioffi GA. Intravitreal colchicine causes decreased RNFL birefringence without altering RNFL thickness. *Invest Ophthalmol Vis Sci*. 2008;49:255–261.
18. Huang XR, Bagga H, Greenfield DS, Knighton RW. Variation of peripapillary retinal nerve fiber layer birefringence in normal human subjects. *Invest Ophthalmol Vis Sci*. 2004;45:3073–3080.
19. Kashiwagi K, Ou B, Nakamura S, Tanaka Y, Suzuki M, Tsukahara S. Increase in dephosphorylation of the heavy neurofilament subunit in the monkey chronic glaucoma model. *Invest Ophthalmol Vis Sci*. 2003;44:154–159.
20. Balaratnasingam C, Morgan WH, Bass L, Matich G, Cringle SJ, Yu DY. Axonal transport and cytoskeletal changes in the laminar regions after elevated intraocular pressure. *Invest Ophthalmol Vis Sci*. 2007;48:3632–3644.
21. Balaratnasingam C, Morgan WH, Bass L, Cringle SJ, Yu DY. Time-dependent effects of elevated intraocular pressure on

optic nerve head axonal transport and cytoskeleton proteins. *Invest Ophthalmol Vis Sci*. 2008;49:986–999.

22. Huang XR, Knighton RW. Altered F-actin distribution in retinal nerve fiber layer of a rat model of glaucoma. *Exp Eye Res*. 2009;88:1107–1114.
23. Huang X, Kong W, Zhou Y, Gregori G. Distortion of axonal cytoskeleton: an early sign of glaucomatous damage. *Invest Ophthalmol Vis Sci*. 2011;52:2879–2888.
24. Vickers JC, Schumer RA, Podos SM, Wang RF, Riederer BM, Morrison JH. Differential vulnerability of neurochemically identified subpopulations of retinal neurons in a monkey model of glaucoma. *Brain Res*. 1995;680:23–35.
25. Soto I, Pease ME, Son JL, Shi X, Quigley HA, Marsh-Armstrong N. Retinal ganglion cell loss in a rat ocular hypertension model is sectorial and involves early optic nerve axon loss. *Invest Ophthalmol Vis Sci*. 2011;52:434–441.
26. Cense B, Chen TC, Park BH, Pierce MC, de Boer JF. Invivo depth-resolved birefringence measurements of the human retinal nerve fiber layer by polarization-sensitive optical coherence tomography. *Opt Lett*. 2002;27:1610–1612.
27. Cense B, Chen TC, Park BH, Pierce MC, de Boer JF. Thickness and birefringence of healthy retinal nerve fiber layer tissue measured with polarization-sensitive optical coherence tomography. *Invest Ophthalmol Vis Sci*. 2004;45:2606–2612.
28. Rylander HG III, Kemp NJ, Park J, Zaatari HN, Milner TE. Birefringence of the primate retinal nerve fiber layer. *Exp Eye Res*. 2005;81:81–89.
29. Cense B, Mujat M, Chen TC, Park BH, de Boer JF. Polarization-sensitive spectral-domain optical coherence tomography using a single line scan camera. *Optics Express*. 2007;15:2421–2431.
30. Fortune B, Cull GA, Burgoyne CF. Relative course of retinal nerve fiber layer birefringence and thickness and retinal function changes after optic nerve transection. *Invest Ophthalmol Vis Sci*. 2008;49:4444–4452.
31. Bellezza AJ, Rintalan CJ, Thompson HW, Downs JC, Hart RT, Burgoyne CF. Deformation of the lamina cribrosa and anterior scleral canal wall in early experimental glaucoma. *Invest Ophthalmol Vis Sci*. 2003;44:623–637.
32. Burgoyne CF, Downs JC, Bellezza AJ, Suh JK, Hart RT. The optic nerve head as a biomechanical structure: a new paradigm for understanding the role of IOP-related stress and strain in the pathophysiology of glaucomatous optic nerve head damage. *Prog Retin Eye Res*. 2005;24:39–73.
33. Yang H, Williams G, Downs JC, et al. Posterior (outward) migration of the lamina cribrosa and early cupping in monkey experimental glaucoma. *Invest Ophthalmol Vis Sci*. 2011;52:7109–7121.
34. Strouthidis NG, Fortune B, Yang H, Sigal IA, Burgoyne CF. Longitudinal change detected by spectral domain optical coherence tomography in the optic nerve head and peripapillary retina in experimental glaucoma. *Invest Ophthalmol Vis Sci*. 2011;52:1206–1219.
35. Heickell AG, Bellezza AJ, Thompson HW, Burgoyne CF. Optic disc surface compliance testing using confocal scanning laser tomography in the normal monkey eye. *J Glaucoma*. 2001;10:369–382.
36. Yang H, Thompson H, Roberts MD, Sigal IA, Downs JC, Burgoyne CF. Deformation of the early glaucomatous monkey optic nerve head connective tissue after acute IOP elevation in 3-D histomorphometric reconstructions. *Invest Ophthalmol Vis Sci*. 2011;52:345–363.
37. Strouthidis NG, Fortune B, Yang H, Sigal IA, Burgoyne CF. Effect of acute intraocular pressure elevation on the monkey optic nerve head as detected by spectral domain optical coherence tomography. *Invest Ophthalmol Vis Sci*. 2011;52:9431–9437.
38. Strouthidis NG, White ET, Owen VM, Ho TA, Garway-Heath DF. Improving the repeatability of Heidelberg retina tomograph and Heidelberg retina tomograph II rim area measurements. *Br J Ophthalmol*. 2005;89:1433–1437.
39. Fortune B, Wang L, Cull G, Cioffi GA. Intravitreal colchicine causes decreased RNFL birefringence without altering RNFL thickness. *Invest Ophthalmol Vis Sci*. 2007;48:in press.
40. Fortune B, Yang H, Strouthidis NG, et al. The effect of acute intraocular pressure elevation on peripapillary retinal thickness, retinal nerve fiber layer thickness, and retardance. *Invest Ophthalmol Vis Sci*. 2009;50:4719–4726.
41. Weinreb RN, Bowd C, Zangwill LM. Scanning laser polarimetry in monkey eyes using variable corneal polarization compensation. *J Glaucoma*. 2002;11:378–384.
42. Choplin NT, Zhou Q, Knighton RW. Effect of individualized compensation for anterior segment birefringence on retinal nerve fiber layer assessments as determined by scanning laser polarimetry. *Ophthalmology*. 2003;110:719–725.
43. GDxVCC Instrument Manual. *RNFL Analysis with GDxVCC: A Primer and Clinical Guide*. San Diego, CA: Laser Diagnostic Technologies, Inc; 2004.
44. Fortune B, Wang L, Bui BV, Cull G, Dong J, Cioffi GA. Local ganglion cell contributions to the macaque electroretinogram revealed by experimental nerve fiber layer bundle defect. *Invest Ophthalmol Vis Sci*. 2003;44:4567–4579.
45. Fortune B, Wang L, Bui BV, Burgoyne CF, Cioffi GA. Idiopathic bilateral optic atrophy in the rhesus macaque. *Invest Ophthalmol Vis Sci*. 2005;46:3943–3956.
46. Gaasterland D, Kupfer C. Experimental glaucoma in the rhesus monkey. *Invest Ophthalmol*. 1974;13:455–457.
47. Quigley HA, Hohman RM. Laser energy levels for trabecular meshwork damage in the primate eye. *Invest Ophthalmol Vis Sci*. 1983;24:1305–1307.
48. Chauhan BC, Blanchard JW, Hamilton DC, LeBlanc RP. Technique for detecting serial topographic changes in the optic disc and peripapillary retina using scanning laser tomography. *Invest Ophthalmol Vis Sci*. 2000;41:775–782.
49. Chauhan BC, McCormick TA, Nicolela MT, LeBlanc RP. Optic disc and visual field changes in a prospective longitudinal study of patients with glaucoma: comparison of scanning laser tomography with conventional perimetry and optic disc photography. *Arch Ophthalmol*. 2001;119:1492–1499.
50. Rangaswamy NV, Zhou W, Harwerth RS, Frishman LJ. Effect of experimental glaucoma in primates on oscillatory potentials of the slow-sequence mfERG. *Invest Ophthalmol Vis Sci*. 2006;47:753–767.
51. Ventura LM, Porciatti V. Restoration of retinal ganglion cell function in early glaucoma after intraocular pressure reduction: a pilot study. *Ophthalmology*. 2005;112:20–27.
52. Ventura LM, Feuer WJ, Porciatti V. Progressive loss of retinal ganglion cell function is hindered with IOP-lowering treatment in early glaucoma. *Invest Ophthalmol Vis Sci*. 2012;53:659–663.
53. Roberts MD, Grau V, Grimm J, et al. Remodeling of the connective tissue microarchitecture of the lamina cribrosa in early experimental glaucoma. *Invest Ophthalmol Vis Sci*. 2009;50:681–690.
54. Howell GR, Libby RT, Jakobs TC, et al. Axons of retinal ganglion cells are insulted in the optic nerve early in DBA/2J glaucoma. *J Cell Biol*. 2007;179:1523–1537.
55. Soto I, Oglesby E, Buckingham BP, et al. Retinal ganglion cells downregulate gene expression and lose their axons within the optic nerve head in a mouse glaucoma model. *J Neurosci*. 2008;28:548–561.
56. Buckingham BP, Inman DM, Lambert W, et al. Progressive ganglion cell degeneration precedes neuronal loss in a mouse model of glaucoma. *J Neurosci*. 2008;28:2735–2744.
57. Salinas-Navarro M, Alarcon-Martinez L, Valiente-Soriano FJ, et al. Ocular hypertension impairs optic nerve axonal transport

leading to progressive retinal ganglion cell degeneration. *Exp Eye Res*. 2010;90:168–183.

58. Crish SD, Sappington RM, Inman DM, Horner PJ, Calkins DJ. Distal axonopathy with structural persistence in glaucomatous neurodegeneration. *Proc Natl Acad Sci U S A*. 2010;107:5196–5201.
59. Sihota R, Sony P, Gupta V, Dada T, Singh R. Diagnostic capability of optical coherence tomography in evaluating the degree of glaucomatous retinal nerve fiber damage. *Invest Ophthalmol Vis Sci*. 2006;47:2006–2010.
60. Chan CK, Miller NR. Peripapillary nerve fiber layer thickness measured by optical coherence tomography in patients with no light perception from long-standing nonglaucomatous optic neuropathies. *J Neuroophthalmol*. 2007;27:176–179.
61. Zhou W, Rangaswamy N, Ktonas P, Frishman LJ. Oscillatory potentials of the slow-sequence multifocal ERG in primates extracted using the Matching Pursuit method. *Vision Res*. 2007;47:2021–2036.
62. Luo X, Patel NB, Harwerth RS, Frishman LJ. Loss of the low-frequency component of the global-flash multifocal electroretinogram in primate eyes with experimental glaucoma. *Invest Ophthalmol Vis Sci*. 2011;52:3792–3804.
63. Anderson DR, Hendrickson A. Effect of intraocular pressure on rapid axoplasmic transport in monkey optic nerve. *Invest Ophthalmol*. 1974;13:771–783.
64. Quigley H, Anderson DR. The dynamics and location of axonal transport blockade by acute intraocular pressure elevation in primate optic nerve. *Invest Ophthalmol*. 1976;15:606–616.
65. Minckler DS, Bunt AH, Klock IB. Radioautographic and cytochemical ultrastructural studies of axoplasmic transport in the monkey optic nerve head. *Invest Ophthalmol Vis Sci*. 1978;17:33–50.
66. Quigley HA, Guy J, Anderson DR. Blockade of rapid axonal transport. Effect of intraocular pressure elevation in primate optic nerve. *Arch Ophthalmol*. 1979;97:525–531.
67. Quigley HA, Addicks EM. Chronic experimental glaucoma in primates. II. Effect of extended intraocular pressure elevation on optic nerve head and axonal transport. *Invest Ophthalmol Vis Sci*. 1980;19:137–152.
68. Martin KR, Quigley HA, Valenta D, Kielczewski J, Pease ME. Optic nerve dynein motor protein distribution changes with intraocular pressure elevation in a rat model of glaucoma. *Exp Eye Res*. 2006;83:255–262.
69. McKendrick AM, Badcock DR, Morgan WH. Psychophysical measurement of neural adaptation abnormalities in magnocellular and parvocellular pathways in glaucoma. *Invest Ophthalmol Vis Sci*. 2004;45:1846–1853.
70. Sun H, Swanson WH, Arvidson B, Dul MW. Assessment of contrast gain signature in inferred magnocellular and parvocellular pathways in patients with glaucoma. *Vision Res*. 2008;48:2633–2641.
71. Redmond T, Garway-Heath DF, Zlatkova MB, Anderson RS. Sensitivity loss in early glaucoma can be mapped to an enlargement of the area of complete spatial summation. *Invest Ophthalmol Vis Sci*. 2010;51:6540–6548.
72. Hackett DA, Anderson AJ. Determining mechanisms of visual loss in glaucoma using Rarebit perimetry. *Optom Vis Sci*. 2011;88:48–55.
73. Yucel Y, Gupta N. Glaucoma of the brain: a disease model for the study of transsynaptic neural degeneration. *Prog Brain Res*. 2008;173:465–478.
74. Huang XR, Knighton RW, Cavuoto LN. Microtubule contribution to the reflectance of the retinal nerve fiber layer. *Invest Ophthalmol Vis Sci*. 2006;47:5363–5367.
75. Huang XR, Zhou Y, Kong W, Knighton RW. Reflectance decreases before thickness changes in the retinal nerve fiber layer in glaucomatous retinas. *Invest Ophthalmol Vis Sci*. 2011;52:6737–6742.
76. Zhang X, Hu J, Knighton RW, Huang XR, Puliafito CA, Jiao S. Dual-band spectral-domain optical coherence tomography for in vivo imaging the spectral contrasts of the retinal nerve fiber layer. *Opt Express*. 2011;19:19653–19659.
77. van der Schoot J, Vermeer KA, de Boer JF, Lemij HG. The effect of glaucoma on the optical attenuation coefficient of the retinal nerve fiber layer in spectral domain optical coherence tomography images. *Invest Ophthalmol Vis Sci*. 2012;53:2424–2430.